ADVANCED FUNCTIONAL MATERIALS

Supporting Information

for *Adv. Funct. Mater.,* DOI: 10.1002/adfm.202100880

Transparent and Flexible $Mn_{1-x-y}(Ce_xLa_y)O_{2-\delta}$ Ultrathin-Film Device for Highly-Stable Pseudocapacitance Application

Samane Maroufi, Rasoul Khayyam Nekouei, Sajjad S. Mofarah, Anthony P. O'Mullane, Yin Yao, Sean Lim, Claudio Cazorla, and Veena Sahajwalla*

WILEY-VCH

Supplementary Information

Transparent and Flexible $Mn_{1-x-y}(Ce_xLa_y)O_{2-\delta}$ Ultrathin-Film Device for Highly-Stable Pseudocapacitance Application

Samane Maroufi[1], Rasoul Khayyam Nekouei[1§], Sajjad S. Mofarah[1§], Anthony P. O'Mullane[2], Yin Yao[3], Sean Lim[3], Claudio Cazorla[4],and Veena Sahajwalla[1]*

[1] Centre for Sustainable Materials Research and Technology, SMaRT@UNSW, School of Materials Science and Engineering, UNSW Sydney, NSW 2052, Australia

[2] School of Chemistry and Physics, Queensland University of Technology (QUT), Brisbane, QLD 4001, Australia

[3] Electron Microscopy Unit (EMU)Mark Wainwright Analytical Centre UNSW Sydney, Australia

[4] Department of Physics, Polytechnic University of Catalonia, Spain

[*] Corresponding author, Email: s.maroufi@unsw.edu.au

[§] Authors have equal contributions.

1. Materials and Methods

1.1 Experimental Procedure

A nitric based-precursor containing Ce, La, and Mn ions was prepared from the dissolution of electronic waste materials, followed by purification steps. The elemental composition of the precursor was analysed by inductively coupled plasma optical emission spectroscopy (ICP-OES, Perkin Elmer Optima DV7300), and is available in **Table S1**, showing the remarkable high concentration of La and Ce compared to Mn, with the ratio of 63:7.5:0.9, respectively. The ppm concentration of Mn is due to the fact that Mn removal was the last step of purification for the extraction of rare earth oxides (REOs) from the precursor in the recycling process. This trace amount of Mn was deposited using chronoamperometry technique, via a potentiostat/galvanostat (VSP-300, BioLogic) workstation, on the surface of fluorine-doped tin oxide (FTO) coated glass with the exposed surface area of 1.8-1.9 cm^2. Before the deposition, the FTO substrate was carefully rinsed with ethanol, acetone, and deionised water in a sonicator. Electrodeposition experiments were conducted using a three-electrode configuration, in which FTO was used as working electrode (WE), a Pt spiral wire as the counter electrode (CE), and standard calomel electrode (SCE) as the reference electrode (RE). Thin films were electrodeposited from the solution at 70°C, since at this temperature the rapid extraction of Mn resulted in the formation of an adherent and smooth thin-film. The electrodeposition potential was kept constant at 1.0 V vs. SCE to pass a specific amount of electric charge (in mC) for every cm^2 of area; hence, the deposited weight in all samples was comparable. After electrodeposition, the prepared electrode was thoroughly rinsed by distilled water and dried in ambient air. To double-check the deposited weight, some samples were weighted using a five-digit microbalance with the accuracy of ±10 µg.

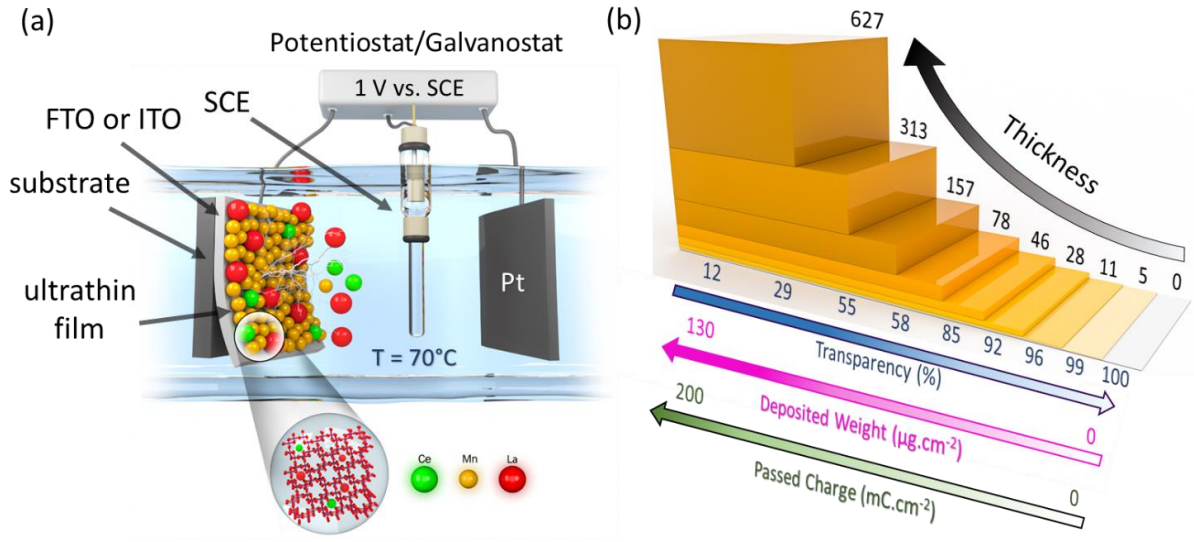

Figure S1. Schematic of **(a)** the chronoamperometric synthesis of $Mn_{1-x-y}(Ce_xLa_y)O_{2-\delta}$ ultrathin films on FTO, and **(b)** the resultant $Mn_{1-x-y}(Ce_xLa_y)O_{2-\delta}$ ultrathin films at different thicknesses.

Table S1. ICP Elemental analysis of the precursor for $Mn_{1-x-y}(Ce_xLa_y)O_{2-\delta}$ electrodeposition.

Element	**Ce**	**Fe**	**La**	**Mn**	**Nd**	**Ni**	**Pr**
Concentration ($mg.L^{-1}$)	7571	0.35	63160	860	4604	698	1287

For comparing the results of ultrathin films made of $Mn_{1-x-y}(Ce_xLa_y)O_{2-\delta}$, ultrathin films made of MnO_{2-x} were also fabricated. The precursor for the MnO_{2-x} films was prepared from the leaching of pure metallic Mn (extracted from the recycling of spent zinc-manganese oxide batteries) in the glacial acetic acid. The concentration of Mn and pH of the solution were 4.6 g.L and 5.0, respectively.

The electrochemical performance of the as-synthesised thin-film was examined in 2 M KOH aqueous solution using a three-electrode cell configuration at room temperature. Cyclic voltammetry (CV) and galvanostatic charge-discharge (GCD) tests were performed in the range of -0.3 to 0.5 vs. SCE/V using the three-electrode cell configuration in which the thin-film electrode was used as the WE. Electrochemical impedance spectroscopy (EIS) was conducted at 0.0 vs. SCE/V and 10 mV of amplitude between 100 kHz to 100 mHz, after leaving the working electrode in the solution for 20 min to reach a constant open circuit potential (OCP).

To access the performance of the optimum $Mn_{1-x-y}(Ce_xLa_y)O_{2-\delta}$ thin-films in a two-electrode system, the CE and RE were replaced by a similar WE to make a symmetric capacitor. In the second step of development, a solid-state device was fabricated including two identical thin-films coated on two FTOs and solid-state LiCl/PVA electrolyte as an interlayer. The solid-state gel electrolyte was made after thoroughly mixing (via a magnet stirrer) of 0.43 g LiCl, 1 g PVA, and 10 ml deionised water at 85 °C for around 1 hr. Small droplets of gel electrolyte, enough to cover the whole surface, was applied on the surface of both films and two FTOs were gently squeezed together under a mild presser using paper clips for 24 hr. In the third step of development, the optimum thin-film was electrodeposited on the surface of indium tin oxide (ITO) coated polyethylene terephthalate (PET) flexible substrate with the resistance of 30 Ω.square^{-1}. Prior to deposition, the ITO coated PET was washed and treated in acetone, ethanol, and deionised water before electrolytic deposition. The deposition procedure was similar to that of FTO. These three symmetric devices were employed for electrochemical analysis. The energy density (E) and power density (P) of the two-electrode device were calculated using the following equations[1]:

$$E\ (\text{wh kg}^{-1}) = \frac{C \times (\Delta V)^2}{7.2} \quad \text{(Eq. S1)}$$

$$P\ (\text{W kg}^{-1}) = \frac{3600 \times E}{\Delta t} \quad \text{(Eq. S2)}$$

Where C (F.g^{-1}) is the specific capacitance, ΔV (V) is the potential window, and Δt (s) is the discharge duration in CD analysis.

1.2 Advanced characterisation equipment and parameters

The morphology of samples was observed by field-emission scanning electron microscopy (FE-SEM, NanoSEM 450 NOVA). Raman data were obtained by a Renishaw inVia Raman microscope (Gloucestershire, UK), which is equipped with a He-Ne green laser (λ=514 nm) and diffraction grating of 1800 g mm^{-1}. Before characterisation, the equipment was calibrated against the Si peak at ~520 cm^{-1}. The Raman spectra were obtained for the range 100-800 cm^{-1} and spot size ~4 µm. The data were analysed by Renishaw WiRE 4.4 software. Transparency and bandgap of the films were analysed using ultraviolet-visible spectroscopy (UV–Vis, Perkin Elmer Lambda 35 equipped with UV Winlab V.6 software) in the presence of FTO coated glass as the standard sample. The bandgap of samples calculated using well-known Kubelka-Munk function and illustrated in a Tauc plot. To find out the chemical state and oxidation number of elements, X-ray photoelectron spectrometer (XPS, Thermo Scientific ESCALAB250i with monochromated Al Kα line (1486.68 eV) as the X-ray source) analysis was utilised under high vacuum (2–9 mbar) with 20 eV passing energy. The thickness and composition of the films were subjected to time-of-flight secondary ion mass spectroscopy (TOF-SIMS) under positive polarity by Bi_3^+ at 30 KeV and sputtered by Cs^+ beam of 1000 eV. EPR analysis was implemented using a Bruker EMX X-Band ESR Spectrometer with a constant frequency at 9.8520 GHz. The corresponding data were obtained at centre Field of 3400 mT, modulation amplitude at 4G,

and microwave power of 20 mW. Further, the EPR signal and hyperfine processing were carried out using Bruker Xenon software.

In all advanced characterisation methods expect EPR, thin films were directly used. The powder samples for EPR analysis were prepared by scratching the surface of films using a sharp knife.

1.3 DFT calculations

Spin-polarized density functional theory (DFT) [2] calculations were performed to theoretically characterise the electronic band properties of the α, β, and δ polymorphs of MnO_2 as well as of Ce/La inserted α-MnO_2. The PBEsol+U exchange-correlation energy functional [3] was used as it is implemented in the VASP software [4]. A "Hubbard-U" scheme [5] with U = 3 eV was employed for better treatment of the localized Mn 3d and Ce 4f electronic orbitals. We employed the "projector augmented wave" method [6] to represent the ionic cores by considering the following electrons as valence: Mn 3d and 4s; O 2s and 2p; Ce 4f, 5d, 6s, and 4d; and La 5d, 6s, and 4d. Wave functions were represented in a plane-wave basis truncated at 650 eV. For integrations within the first Brillouin zone, we employed Monkhorst-Pack k-point grids with a density equivalent to that of a 10x10x16 mesh for the bulk β-MnO_2 unit cell. Periodic boundary conditions were applied along the three lattice vectors defining the simulation supercell. Geometry relaxations were performed with a conjugate-gradient algorithm that optimised the ionic positions and volume and shape of the simulation cell. The relaxations were halted when the forces in the atoms wereall below 0.01 eV·Å^{-1}. By using these technical parameters, total energies were converged to within 0.5 meV per formula unit. The range-separated hybrid HSE06 exchange-correlation functional [7] was used to accurately estimate the electronic properties of the equilibrium geometries determined at the PBEsol+U level.

2. Results

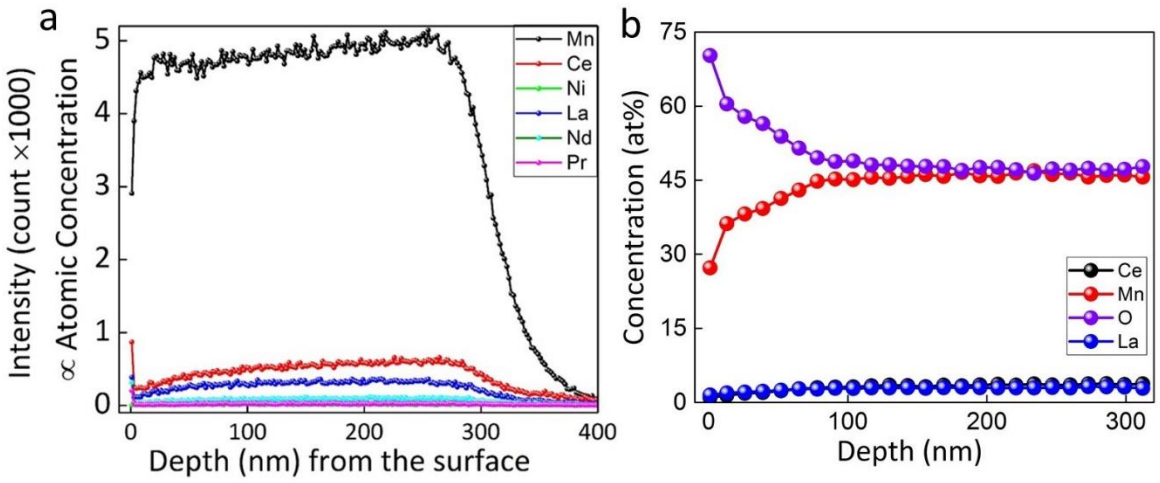

Figure S2. (**a)** Depth profile of the concentration of various elements present in $Mn_{1-x-y}(Ce_xLa_y)O_{2-\delta}$ film taken by TOF-SIMS, and (**b)** concentration of various elements present in $Mn_{1-x-y}(Ce_xLa_y)O_{2-\delta}$ film along the thin film taken by XPS.

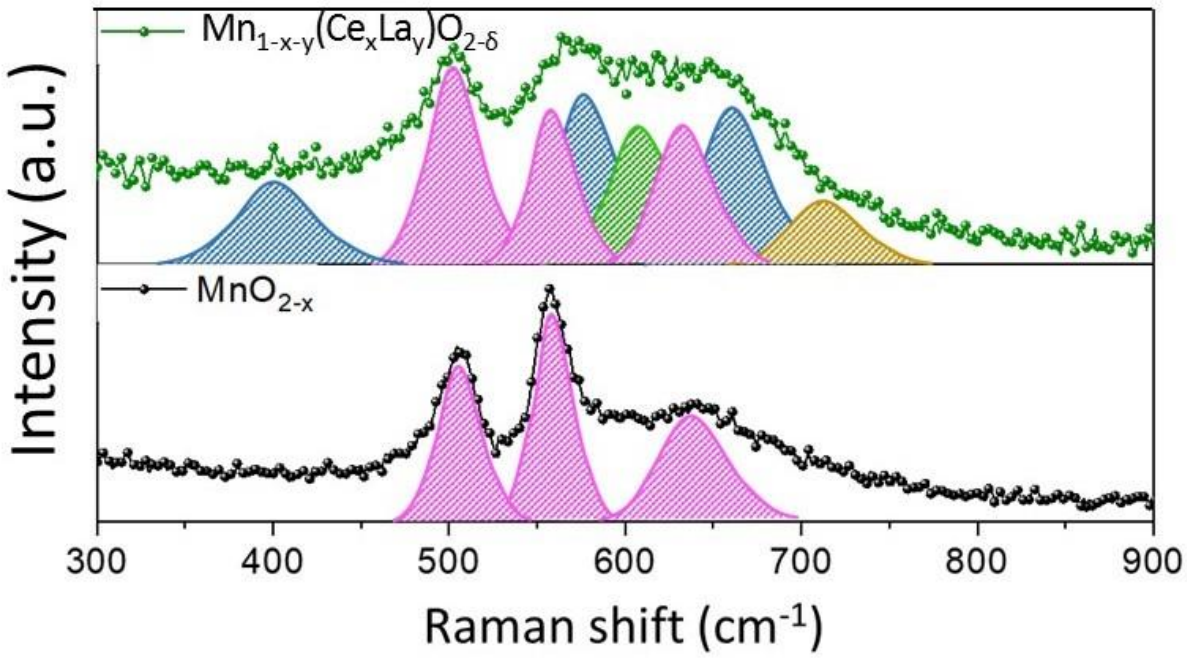

Figure S3. Raman spectrum of the as-fabricated MnO_{2-x} and $Mn_{1-x-y}(Ce_xLa_y)O_{2-\delta}$ films.

Table S2. Electron paramagnetic resonance (EPR) data for $Mn_{1-x-y}(Ce_xLa_y)O_{2-\delta}$ film.

Sample	MWFQ (GHz)*	Hyperfines (mT)					g-Factors				
La-Ce-MnO_{2-zx}	9.852088	325.44	329.52	334.48	338.36	343.71	2.16	2.12	2.10	2.08	2.05
		347.80	351.35	353.23	357.30	363.14	2.016	2.005	2.00	1.96	1.93
		367.12	373.15	377.76			1.91	1.88	1.86		

* The microwave frequencies (MWFQ) of the samples kept constant so as to enable to carry out quantification analysis of structural defects.

Table S3. Detailed figures for the characteristics of the as-synthesised thin-film $Mn_{1-x-y}(Ce_xLa_y)O_{2-\delta}$ electrodes.

Sample Number	Deposited/passed charge ($mC.cm^{-2}$)	Deposited weight ($\mu g.cm^{-2}$)	Thickness (nm)	Transparency (%) at 550 nm (compared to FTO)	Mean Transparency between 400 to 800 nm (compared to FTO)
Bare FTO	0	0	-	100	100
I	1.56	1.01	5	99.7	98.6
II	3.13	2.03	11	95.7	93.6
III	6.25	4.06	28	91.9	89.5
IV	12.5	8.13	46	85.1	83.2
V	25	16.3	78	58.5	59.5
VI	50	32.5	157	54.8	52.3
VII	100	65	313	28.9	37.3
VIII	200	130	627	12.0	27.9

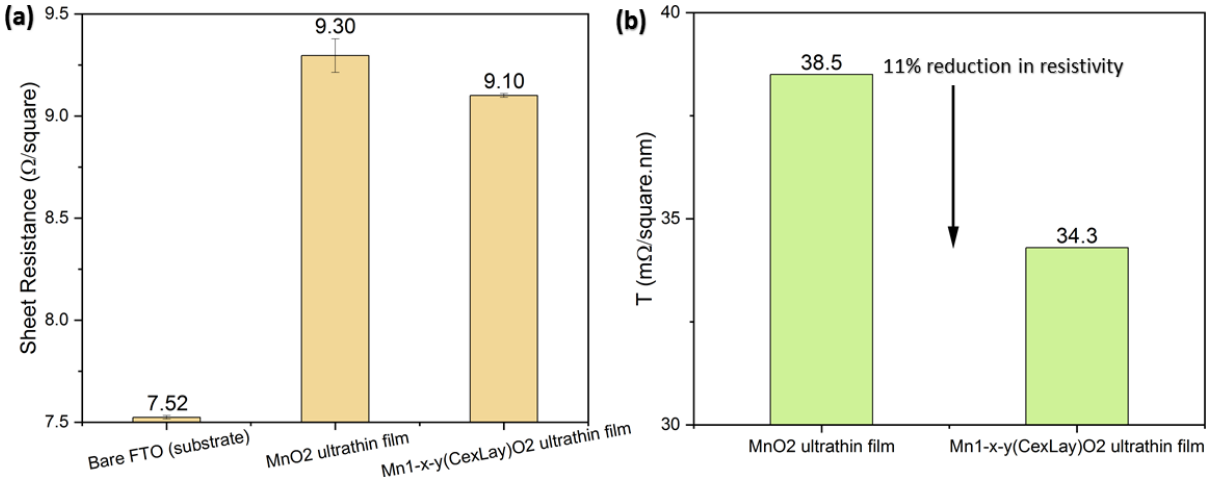

Figure S4. Results of four-point probe resistivity analysis using ultrathin films with optimum conditions in thickness of 46 nm; **(a)** bar charts of resistivity for FTO substrate, MnO_{2-x}, and $Mn_{1-x-y}(Ce_xLa_y)O_{2-\delta}$ ultrathin films deposited on FTO, and **(b)** normalised resistivity values based on the thickness.

Table S4. *A comparative study on specific capacitances of flexible, transparent, and ultrathin films reported to date with that obtained in the present work.*

Electrode Materials	*Transparency (%) @ λ (at 550 nm)*	*Areal Capacitance*	*Gravimetric Capacitance*	*Cycling stability (%) – cycle number*	*Published Journal*	*Year Published*	*Ref.*
Flexible, Transparent Ultrathin Film							
RuO_2/PEDOT (Symmetric)	80%	0.88 mF.cm^{-2}	-	80% after 10,000	Nano Energy	2016	[8]
RuO_2/PEDOT (Asymmetric)	78%	1.06 mF.cm^{-2}	-	93% after 6,000	Nano Energy	2016	[8]
Graphene	72%	6.0 μF.cm^{-2}	-	100% after 10,000	ACS Nano	2014	[9]
Carbon nanotubes/V_2O_5	87%	~45 mF.cm^{-2}	-	33% after 100	ACS Nano	2015	[10]
Ni-doped δ-MnO_2	-	-	338 F.g^{-1}	98% after 4,000	ACS Sus. Chem.	2017	[11]
Au/MnO_2	75%	3.23 mF.cm^{-2}	-	92% after 5,000	Small	2017	[12]
Au/ MnO_2 (solid state device)	63%	0.66 mF.cm^{-2}	-	-			
Au/MnO_2	40%-70%	4.7-2 mF.cm^{-2}	-	81% after 500	Small	2015	[13]
Graphene	70%	-	135 F.g^{-1}	-	Applied Physics Letter	2010	[14]
Co_3O_4	51%	6.03 mF.cm^{-2}	170 F.g^{-1}	93% after 30,000	Nanoscale	2016	[15]
MnO_2	44%	4.73 mF.cm^{-2}		88% after 1000	ACS Appl. Mater. Interfaces	2018	[16]
Au/MnO_2	72%	3.68 mF.cm^{-2}	-	96% after 8400	Chem. Eng.	2020	[17]
$Co(OH)_2$/Ag	54%	0.9 mF.cm^{-2}		91% after 10,000	ACS Appl. Mater. Interfaces	2019	[18]
MoO_3 / PEDOT	70%	2.99 mF.cm^{-2}		99% after 2500	ACS Appl. Energy Mater.	2019	[19]
Graphene	46 %	3.3 mF.cm^{-2}	-	95% after 20,000	Nano Lett.	2015	[20]
Graphene	75%	0.1 mF.cm^{-2}	-	-	Chem. Mater.	2015	[21]
$Mn_{1-x-y}(Ce_xLa_y)O_{2-\delta}$	85% @ 550	5.07 mF.cm^{-2}	621 F.g^{-1}	93% after 16,000	***This work***		

Table S5. *A comparative study on the most recent Mn oxide-based powders/thick films reported to date with those obtained in the present work.*

Electrode Materials	*Areal Capacitance*	*Gravimetric Capacitance*	*Cycling stability (%) – cycle number*	*Published Journal*	*Year Published*	*Ref.*
Hierarchical Hollow MnO_2 (3D) - Powder	-	371.2 Fg^{-1}	93.1% after 2000 Cycles	J. Mater. Chem. A	2015	[22]
α-MnO_2/δ-MnO_2 heterojunction - powder	783 mF cm^{-2}	28-178 Fg^{-1}	78.0% after 20,000 cycles	Mater. Horizons	2017	[23]
Cobalt doped MnO_2 - powder	-	350 Fg^{-1}	90.0% after 1000 cycles	J. Phys. Chem. C	2015	[24]
MnO_2 nanoflowers deposited on graphene paper	-	385.2 Fg^{-1}	85.4% after 5000 cycles	ACS Appl. Nano Mater.	2019	[25]
MnO_x@C@MnO_x core-shell heterostructure - powder	-	350 Fg^{-1}	90.0% after 10,000 cycles	Small	2019	[26]
MnHCF-MnO_x	-	467 Fg^{-1}	91.8% after 8000 cycles	Adv. Energy Mater.	2020	[27]
Al-doped MnO_2	-	213F g-1	91.0% after 15,000 cycles	Nano Energy	2015	[28]
Ultrathin Shell MnO_2/Carbon Core	4.93-26.4	-	97.0% after 10,000 cycles	ACS Sustain. Chem. Eng.	2020	[29]
Highly Loaded Carbon Nanotube/MnO_2 Hybrid Films	1.2	300	75.0% after 1600 cycles	Small	2016	[30]
3D nanotube Ni@MnO_2 powder	10.75	-	-	Appl. Surf. Sci.	2019	[31]
Hierarchical TiO_2@MnO_2 nanowall arrays - powder	22.19		85% after 4000 cycles	Inter. J. Hydrogen Energy	2014	[32]
MnO_2/Au nanofiber	3.68	-	95% after 500 cycles	Chem. Eng.	2020	[17]
Core–shell MnO_2@Au nanofiber	8.26		94% after 10,000 cycles	J. Mater. Chem. A	2019	[33]
REE doped MnO_x	5.07 mF.cm^{-2}	621 F.g^{-1}	93% after 16,000	This work		

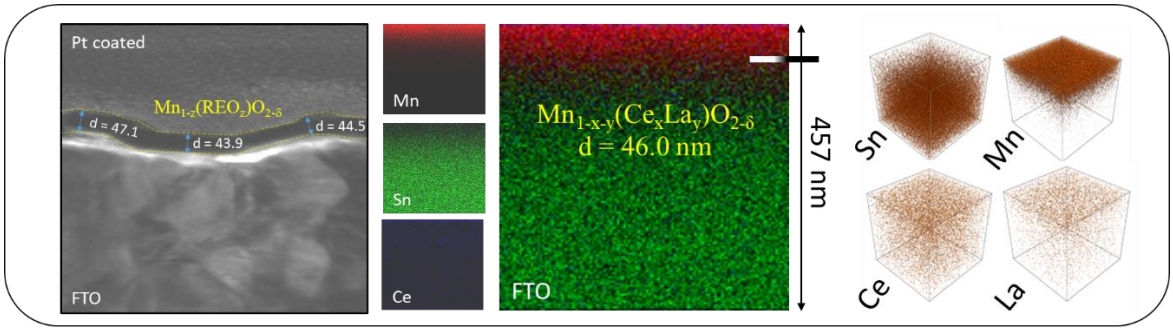

Figure S5. TEM**,** 2D and 3D TOF-SIMS elemental images for the measurement of the thickness, qualitative concentration, and distribution of elements in the as-synthesised film

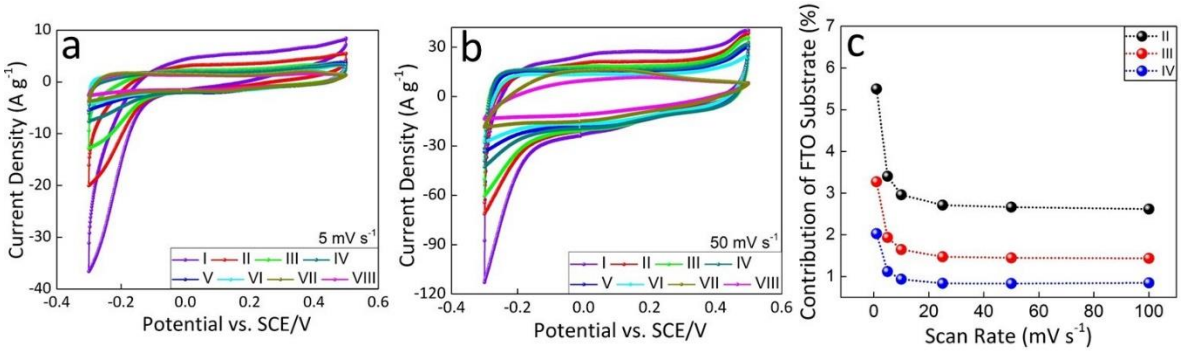

Figure S6 Results of cyclic voltammetry (CV) of the as-synthesised $Mn_{1-x-y}(Ce_xLa_y)O_{2-\delta}$ thin-film electrodes using a three-electrode cell configuration (thin-film electrode as WE, Pt spiral wire as CE, and SCE as RE) at two scan rates of 5 and 50 mV.s^{-1} and in the potential window from -0.3 to 0.5 vs SCE/V in a 2 M KOH aqueous solution; (**a)** normalised gravimetric CVs for the scan rate of 5 mV.s^{-1}; (**b)** normalised gravimetric CVs for the scan rate of 50 mV.s^{-1}, and **c)** contribution of FTO substrate on CV analysis for three electrodes II, III, and IV.

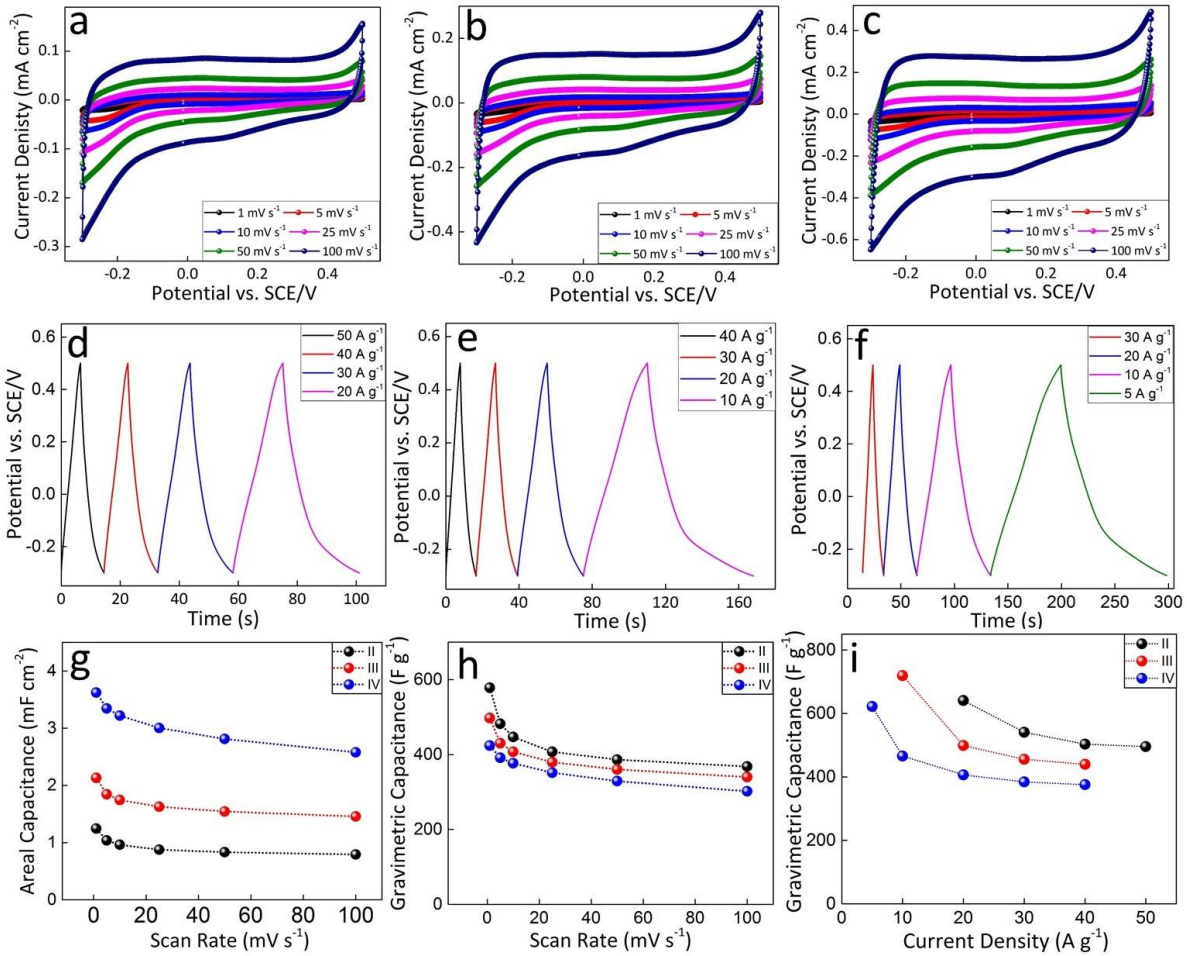

Figure S7 Electrochemical results of the as-synthesised $Mn_{1-x-y}(Ce_xLa_y)O_{2-\delta}$ ultrathin-film electrodes using a three-electrode cell configuration (film electrode as WE, Pt spiral wire as CE, and SCE as RE) in the potential window from -0.3 to 0.5 vs SCE/V in a 2 M KOH aqueous solution. CV of electrodes (**a)** II (5 nm), (**b)** III (28 nm), and (**c)** IV (46 nm) as a function of scan rate; GCD curves for the electrodes (**d)**, II (5 nm), (**e)** III (28 nm), and (**f)** IV (46 nm); (**g)** areal capacitance as a function of scan rate based on CV curves, (**h)** gravimetric capacitance as a function of scan rate based on CV curves; **i)** gravimetric capacitance as a function of current density based on GCD curves for three electrodes II, III, and IV.

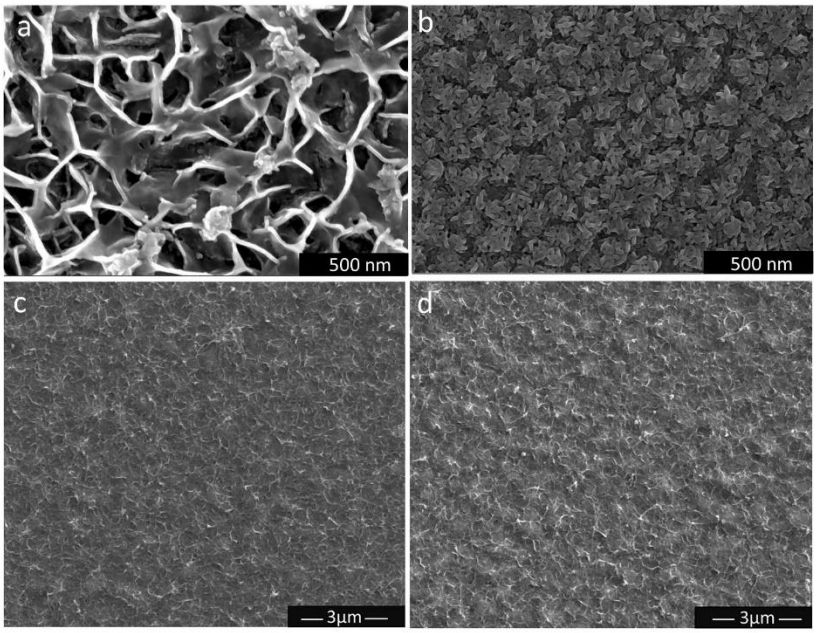

Figure S8. FE-SEM images of the pristine MnO_{2-x} (**a)** as-synthesised, and (**b)** after 2500 cycles; FE-SEM images of $Mn_{1-x-y}(Ce_xLa_y)O_{2-\delta}$ (**c)** as-synthesised, and (**d)** after 16000 cycles.

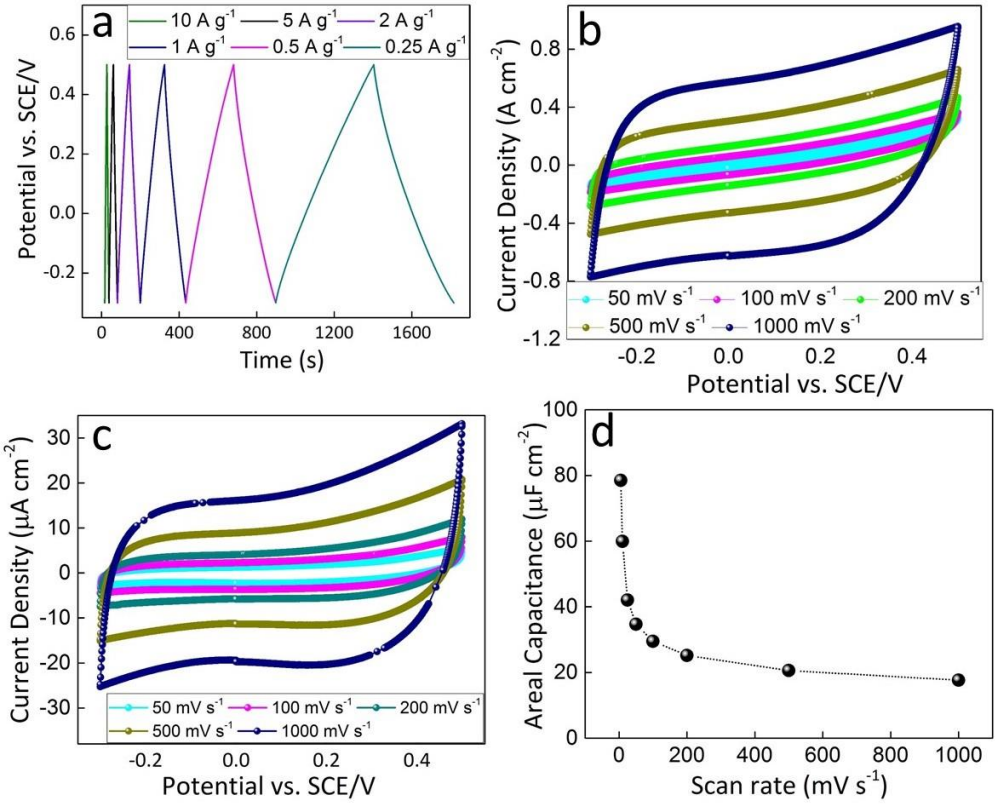

Figure S9. (a) GCD curves of the symmetric two-electrode cell configuration in a 2 M KOH aqueous solution; (**b)** CVs of the symmetric two-electrode configuration using LiCl/PVA solid-state electrolyte and FTO coated glass; (**c)** CVs and **(d)** areal capacitances (as a function of scan rate) of the solid-state symmetric two-electrode cell with ITO coated flexible PET substrate.

Table S6. Table of a comparative study on outstanding specific capacitances reported to date with those obtained in the present work.

Material	*Areal Capacitance ($mF \cdot cm^{-2}$)*	*Gravimetric Capacitance ($F \cdot g^{1}$)*	*Capacitance Retention (%) – Cycle number*	*Published Journal*	*Year Published*	*Ref.*
Three-electrode configuration system						
Reduced graphene oxide (RGO)	N/A	200	91 – 20,000	ChemSusChem	2017	[34]
RGO + carbon dots	N/A	320	89 – 20,000	ChemSusChem	2017	[34]
Graphene oxide + carbon spheres	N/A	272	95 - 500	Carbon	2020	[35]
Graphene oxide + carbon dots	N/A	374	93 – 10,000	Mater. Today Energy	2019	[36]
RGO + active carbon	N/A	541	98 - 8000	J. Power Sources	2020	[37]
RGO + carbon nanotube (CNT)	N/A	272	81 - 2000	Electrochimica Acta	2015	[38]
RGO	N/A	185	N/A	Nano Energy	2015	[39]
Graphene nanomesh + CNT	N/A	294	93 - 5000	Nano Energy	2015	[39]
Nitrogen, phosphorus co-doped graphene framework	N/A	245	95 - 3000	Chem. Eng. J.	2017	[40]
Porous carbon nanosheet + MnO_2	N/A	438	91 – 10,000	ACS Sustainable Chem. Eng.	2019	[41]
Highly functionalised active carbon	0.045	556	93 – 10,000	Energy and Environmental Science	2014	[42]
Active carbon	0.009	180	N/A	Energy and Environmental Science	2014	[42]
REE-MnO_2	**5.0**	**600**	**85 – 16,000**	**-**		**This work**
Two-electrode configuration system (asymmetric and symmetric devices)						
Electrode Materials	***Areal Capacitance ($mF \cdot cm^{-2}$)***	***Gravimetric Capacitance ($F \cdot g^{1}$)***	***Capacitance Retention (%) – Cycle number***	***Published Journal***	***Year Published***	***Ref.***
RGO + active carbon	N/A	116	97.8 - 8000	J. Power Sources	2020	[37]
Graphene	0.2	N/A	77 – 11,000	ACS Nano	2017	[43]
Graphene	0.7	N/A	77 – 11,000	ACS Nano	2017	[43]

Active carbon + Ni-Co-Fe layered double hydroxide	N/A	184	91 - 5000	Energy Storage Mater.	2018	[44]
Active carbon + Ni hydroxide	N/A	153	81 – 10,000	Nat. Commun.	2013	[45]
MnO_2 + graphene hydrogel	N/A	80	75 - 2000	ACS applied Mater. Inter.	2018	[46]
Graphene hydrogel	N/A	10	100 - 2000	ACS applied Mater. Inter.	2018	[46]
MnO_2 + Ti_3C_2	80	112	87 – 10,000	ACS Nano	2020	[47]
RuO_2 + $Ti_3C_2T_x$	N/A	92	86 – 20,000	Adv. Energy. Mater.	2018	[48]
REE-MnO_2	**1.2**	**160**	**85 – 16,000**	**-**		**This work**

References

[1] S. Zhang, N. Pan, Supercapacitors Performance Evaluation, Adv. Energy Mater. 5 (2015) 1401401. doi:10.1002/aenm.201401401.

[2] C. Cazorla, J. Boronat, Simulation and understanding of atomic and molecular quantum crystals, Rev. Mod. Phys. 89 (2017) 35003. doi:10.1103/RevModPhys.89.035003.

[3] J.P. Perdew, A. Ruzsinszky, G.I. Csonka, O.A. Vydrov, G.E. Scuseria, L.A. Constantin, X. Zhou, K. Burke, Restoring the Density-Gradient Expansion for Exchange in Solids and Surfaces, Phys. Rev. Lett. 100 (2008) 136406. doi:10.1103/PhysRevLett.100.136406.

[4] G. Kresse, J. Furthmüller, Efficient iterative schemes for ab initio total-energy calculations using a plane-wave basis set, Phys. Rev. B. 54 (1996) 11169–11186. doi:10.1103/PhysRevB.54.11169.

[5] S.L. Dudarev, G.A. Botton, S.Y. Savrasov, C.J. Humphreys, A.P. Sutton, Electron-energy-loss spectra and the structural stability of nickel oxide: An LSDA+U study, Phys. Rev. B. 57 (1998) 1505–1509. doi:10.1103/PhysRevB.57.1505.

[6] P.E. Blöchl, Projector augmented-wave method, Phys. Rev. B. 50 (1994) 17953–17979. doi:10.1103/PhysRevB.50.17953.

[7] E.N. Brothers, A.F. Izmaylov, J.O. Normand, V. Barone, G.E. Scuseria, Accurate solid-state band gaps via screened hybrid electronic structure calculations, J. Chem. Phys. 129 (2008) 11102. doi:10.1063/1.2955460.

[8] C. Zhang, T.M. Higgins, S.-H. Park, S. O'Brien, D. Long, J. Coleman, V. Nicolosi, Highly flexible and transparent solid-state supercapacitors based on RuO2/PEDOT:PSS conductive ultrathin films, Nano Energy. 28 (2016) 495–505.

[9] P. Xu, J. Kang, J.-B. Choi, J. Suhr, J. Yu, F. Li, J.-H. Byun, B.-S. Kim, T.-W. Chou, Laminated Ultrathin Chemical Vapor Deposition Graphene Films Based Stretchable and Transparent High-Rate Supercapacitor, ACS Nano. 8 (2014) 9437–9445. doi:10.1021/nn503570j.

[10] F.S. Gittleson, D. Hwang, W.-H. Ryu, S.M. Hashmi, J. Hwang, T. Goh, A.D. Taylor, Ultrathin Nanotube/Nanowire Electrodes by Spin–Spray Layer-by-Layer Assembly: A Concept for Transparent Energy Storage, ACS Nano. 9 (2015) 10005–10017. doi:10.1021/acsnano.5b03578.

[11] J. Chen, Y. Liu, G. Wang, J. Guo, X. Wang, Nickel-Doped Ultrathin K-Birnessite Manganese Oxide Nanosheet As Pseudocapacitor Electrode with Excellent Cycling Stability for High-Power Pesudocapacitors, ACS Sustain. Chem. Eng. 5 (2017) 1594–1600. doi:10.1021/acssuschemeng.6b02363.

[12] S. Kiruthika, C. Sow, G.U. Kulkarni, Transparent and Flexible Supercapacitors with Networked Electrodes, Small. 13 (2017) 1701906. doi:10.1002/smll.201701906.

[13] T. Qiu, B. Luo, M. Giersig, E.M. Akinoglu, L. Hao, X. Wang, L. Shi, M. Jin, L. Zhi, Au@MnO2 Core–Shell Nanomesh Electrodes for Transparent Flexible Supercapacitors, Small. 10 (2014) 4136–4141. doi:10.1002/smll.201401250.

[14] A. Yu, I. Roes, A. Davies, Z. Chen, Ultrathin, transparent, and flexible graphene films for supercapacitor application, Appl. Phys. Lett. 96 (2010) 253105. doi:10.1063/1.3455879.

[15] X.Y. Liu, Y.Q. Gao, G.W. Yang, A flexible, transparent and super-long-life supercapacitor based on ultrafine Co3O4 nanocrystal electrodes, Nanoscale. 8 (2016) 4227–4235. doi:10.1039/C5NR09145D.

[16] Y. Wang, W. Zhou, Q. Kang, J. Chen, Y. Li, X. Feng, D. Wang, Y. Ma, W. Huang, Patterning Islandlike MnO2 Arrays by Breath-Figure Templates for Flexible Transparent Supercapacitors, ACS Appl. Mater. Interfaces. 10 (2018) 27001–27008. doi:10.1021/acsami.8b06710.

[17] Y. Lee, S. Chae, H. Park, J. Kim, S.-H. Jeong, Stretchable and transparent supercapacitors based on extremely long MnO2/Au nanofiber networks, Chem. Eng. J. 382 (2020) 122798. doi:https://doi.org/10.1016/j.cej.2019.122798.

[18] H. Sheng, X. Zhang, Y. Ma, P. Wang, J. Zhou, Q. Su, W. Lan, E. Xie, C. Zhang, Ultrathin, Wrinkled, Vertically Aligned Co(OH)2 Nanosheets/Ag Nanowires Hybrid Network for Flexible Transparent Supercapacitor with High Performance., ACS Appl. Mater. Interfaces. 11 9 (2019)

8992–9001.

[19] M. Yoonessi, A. Borenstein, M.F. El-Kady, C.L. Turner, H. Wang, A.Z. Stieg, L. Pilon, Hybrid Transparent PEDOT:PSS Molybdenum Oxide Battery-like Supercapacitors, ACS Appl. Energy Mater. 2 (2019) 4629–4639. doi:10.1021/acsaem.8b02258.

[20] N. Li, G. Yang, Y. Sun, H. Song, H. Cui, G. Yang, C. Wang, Free-Standing and Transparent Graphene Membrane of Polyhedron Box-Shaped Basic Building Units Directly Grown Using a NaCl Template for Flexible Transparent and Stretchable Solid-State Supercapacitors, Nano Lett. 15 (2015) 3195–3203. doi:10.1021/acs.nanolett.5b00364.

[21] K. Jo, S. Lee, S.-M. Kim, J. Bin In, S.-M. Lee, J.-H. Kim, H.-J. Lee, K.-S. Kim, Stacked Bilayer Graphene and Redox-Active Interlayer for Transparent and Flexible High-Performance Supercapacitors, Chem. Mater. 27 (2015) 3621–3627. doi:10.1021/cm504801r.

[22] F. Li, Y. Xing, M. Huang, K.L. Li, T.T. Yu, Y.X. Zhang, D. Losic, MnO2 nanostructures with three-dimensional (3D) morphology replicated from diatoms for high-performance supercapacitors, J. Mater. Chem. A. 3 (2015) 7855–7861. doi:10.1039/C5TA00634A.

[23] C. Zhu, L. Yang, J.K. Seo, X. Zhang, S. Wang, J. Shin, D. Chao, H. Zhang, Y.S. Meng, H.J. Fan, Self-branched α-MnO2/δ-MnO2 heterojunction nanowires with enhanced pseudocapacitance, Mater. Horizons. 4 (2017) 415–422. doi:10.1039/C6MH00556J.

[24] C.-L. Tang, X. Wei, Y.-M. Jiang, X.-Y. Wu, L. Han, K.-X. Wang, J.-S. Chen, Cobalt-Doped MnO2 Hierarchical Yolk–Shell Spheres with Improved Supercapacitive Performance, J. Phys. Chem. C. 119 (2015) 8465–8471. doi:10.1021/jp512795g.

[25] O. Sadak, W. Wang, J. Guan, A.K. Sundramoorthy, S. Gunasekaran, MnO2 Nanoflowers Deposited on Graphene Paper as Electrode Materials for Supercapacitors, ACS Appl. Nano Mater. 2 (2019) 4386–4394. doi:10.1021/acsanm.9b00797.

[26] Z. Ma, F. Jing, Y. Fan, L. Hou, L. Su, L. Fan, G. Shao, High-Stability MnOx Nanowires@C@MnOx Nanosheet Core–Shell Heterostructure Pseudocapacitance Electrode Based on Reversible Phase Transition Mechanism, Small. 15 (2019) 1900862. doi:https://doi.org/10.1002/smll.201900862.

[27] J. Liang, B. Tian, S. Li, C. Jiang, W. Wu, All-Printed MnHCF-MnOx-Based High-Performance Flexible Supercapacitors, Adv. Energy Mater. 10 (2020) 2000022. doi:https://doi.org/10.1002/aenm.202000022.

[28] Z. Hu, X. Xiao, C. Chen, T. Li, L. Huang, C. Zhang, J. Su, L. Miao, J. Jiang, Y. Zhang, J. Zhou, Al-doped α-MnO2 for high mass-loading pseudocapacitor with excellent cycling stability, Nano Energy. 11 (2015) 226–234. doi:https://doi.org/10.1016/j.nanoen.2014.10.015.

[29] C. Kim, J.H. Moon, 3D Bicontinuous Structure of a Pseudocapacitive Ultrathin Shell/Carbon Core: A Novel Electrode for Thin-Film Supercapacitors with High Areal Energy Density, ACS Sustain. Chem. Eng. 8 (2020) 14711–14717. doi:10.1021/acssuschemeng.0c02058.

[30] H. Chen, S. Zeng, M. Chen, Y. Zhang, L. Zheng, Q. Li, Oxygen Evolution Assisted Fabrication of Highly Loaded Carbon Nanotube/MnO2 Hybrid Films for High-Performance Flexible Pseudosupercapacitors, Small. 12 (2016) 2035–2045. doi:https://doi.org/10.1002/smll.201503623.

[31] Y. Chen, S. Xie, G. Li, S. Jia, X. Gao, X. Li, 3D nanotube-structured Ni@MnO2 electrodes: Toward enhanced areal capacitance of planar supercapacitors, Appl. Surf. Sci. 494 (2019) 29–36. doi:https://doi.org/10.1016/j.apsusc.2019.07.063.

[32] A. Ramadoss, S.J. Kim, Hierarchically structured TiO2@MnO2 nanowall arrays as potential electrode material for high-performance supercapacitors, Int. J. Hydrogen Energy. 39 (2014) 12201–12212. doi:https://doi.org/10.1016/j.ijhydene.2014.05.118.

[33] S.B. Singh, T.I. Singh, N.H. Kim, J.H. Lee, A core–shell MnO2@Au nanofiber network as a high-performance flexible transparent supercapacitor electrode, J. Mater. Chem. A. 7 (2019) 10672–10683. doi:10.1039/C9TA00778D.

[34] X. Zhao, M. Li, H. Dong, Y. Liu, H. Hu, Y. Cai, Y. Liang, Y. Xiao, M. Zheng, Interconnected 3 D Network of Graphene-Oxide Nanosheets Decorated with Carbon Dots for High-Performance

Supercapacitors., ChemSusChem. 10 (2017) 2626–2634. doi:10.1002/cssc.201700474.

[35] Z. Wang, Y. Li, J. Liu, T. Gui, H. Ogata, W. Gong, A.K. Vipin, Y. Wang, G.J. Hong Melvin, J. Ortiz-Medina, S. Wang, R. Cruz-Silva, S. Morimoto, Y. Hashimoto, B. Fugetsu, I. Sakata, M. Terrones, M. Endo, Facile synthesis of graphene sheets intercalated by carbon spheres for high-performance supercapacitor electrodes, Carbon N. Y. 167 (2020) 11–18. doi:https://doi.org/10.1016/j.carbon.2020.04.100.

[36] V.C. Hoang, V.G. Gomes, High performance hybrid supercapacitor based on doped zucchini-derived carbon dots and graphene, Mater. Today Energy. 12 (2019) 198–207. doi:https://doi.org/10.1016/j.mtener.2019.01.013.

[37] J. Wang, Q. Li, C. Peng, N. Shu, L. Niu, Y. Zhu, To increase electrochemical performance of electrode material by attaching activated carbon particles on reduced graphene oxide sheets for supercapacitor, J. Power Sources. 450 (2020) 227611. doi:https://doi.org/10.1016/j.jpowsour.2019.227611.

[38] X. Cui, R. Lv, R.U.R. Sagar, C. Liu, Z. Zhang, Reduced graphene oxide/carbon nanotube hybrid film as high performance negative electrode for supercapacitor, Electrochim. Acta. 169 (2015) 342–350. doi:https://doi.org/10.1016/j.electacta.2015.04.074.

[39] S. Byun, B. Shin, Densely packed hybrid films comprising SnO2 and reduced graphite oxide for high-density electrochemical capacitors, J. Mater. Chem. A. 4 (2016) 16175–16183. doi:10.1039/C6TA05494C.

[40] X. Wang, Y. Liu, P. Wu, Water-soluble triphenylphosphine-derived microgel as the template towards in-situ nitrogen, phosphorus co-doped mesoporous graphene framework for supercapacitor and electrocatalytic oxygen reduction, Chem. Eng. J. 328 (2017) 417–427. doi:https://doi.org/10.1016/j.cej.2017.07.064.

[41] B. Liu, Y. Liu, H. Chen, M. Yang, H. Li, MnO2 Nanostructures Deposited on Graphene-Like Porous Carbon Nanosheets for High-Rate Performance and High-Energy Density Asymmetric Supercapacitors, ACS Sustain. Chem. Eng. 7 (2019) 3101–3110. doi:10.1021/acssuschemeng.8b04817.

[42] Z. Li, Z. Xu, H. Wang, J. Ding, B. Zahiri, C.M.B. Holt, X. Tan, D. Mitlin, Colossal pseudocapacitance in a high functionality–high surface area carbon anode doubles the energy of an asymmetric supercapacitor, Energy Environ. Sci. 7 (2014) 1708–1718. doi:10.1039/C3EE43979H.

[43] J. Li, S. Sollami Delekta, P. Zhang, S. Yang, M.R. Lohe, X. Zhuang, X. Feng, M. Östling, Scalable Fabrication and Integration of Graphene Microsupercapacitors through Full Inkjet Printing., ACS Nano. 11 (2017) 8249–8256. doi:10.1021/acsnano.7b03354.

[44] Y. Shabangoli, M.S. Rahmanifar, M.F. El-Kady, A. Noori, M.F. Mousavi, R.B. Kaner, An integrated electrochemical device based on earth-abundant metals for both energy storage and conversion, Energy Storage Mater. 11 (2018) 282–293. doi:https://doi.org/10.1016/j.ensm.2017.09.010.

[45] H.B. Li, M.H. Yu, F.X. Wang, P. Liu, Y. Liang, J. Xiao, C.X. Wang, Y.X. Tong, G.W. Yang, Amorphous nickel hydroxide nanospheres with ultrahigh capacitance and energy density as electrochemical pseudocapacitor materials, Nat. Commun. 4 (2013) 1894. doi:10.1038/ncomms2932.

[46] X. Meng, L. Lu, C. Sun, Green Synthesis of Three-Dimensional MnO2/Graphene Hydrogel Composites as a High-Performance Electrode Material for Supercapacitors, ACS Appl. Mater. Interfaces. 10 (2018) 16474–16481. doi:10.1021/acsami.8b02354.

[47] F. Zhao, W. Liu, T. Qiu, W.-B. Gong, W. Ma, Q. Li, F. Li, F. Geng, All Two-Dimensional Pseudocapacitive Sheet Materials for Flexible Asymmetric Solid-State Planar Microsupercapacitors with High Energy Density, ACS Nano. 14 (2020) 603–610. doi:10.1021/acsnano.9b07183.

[48] Q. Jiang, N. Kurra, M. Alhabeb, Y. Gogotsi, H.N. Alshareef, All Pseudocapacitive MXene-RuO2 Asymmetric Supercapacitors, Adv. Energy Mater. 8 (2018) 1703043.

doi:https://doi.org/10.1002/aenm.201703043.